DOI: 10.1002/chem.201000431

3D–2D–0D Stepwise Deconstruction of a Water Framework Templated by a Nanoporous Organic–Inorganic Hybrid Host

João Rocha,*[a] Fa-Nian Shi,[a] Filipe A. Almeida Paz,[a] Luís Mafra,[a] Mariana Sardo,[a] Luís Cunha-Silva,[a] James Chisholm,[b] Paulo Ribeiro-Claro,[a] and Tito Trindade[a]

Abstract: The supramolecular salt $[H_2pip]_3[Ge(hedp)_2]\cdot 14H_2O$ (**1**) [H_2pip^{2+} = piperazine cation $C_4H_{12}N_2^{2+}$; $hedp^{5-}$ = deprotonated form of etidronic acid, $C_2H_3P_2O_7^{5-}$) is reported. This consists of an organic–inorganic hybrid hydrogen-bonded nanoporous framework, the internal surface of which acts as a template for the three-dimensional (3D) clustering of water molecules. The structure and molecular dynamics of this material are characterised by single-crystal X-ray diffraction, thermogravimetric analysis, Raman (H/D isotopic substitution) spectroscopy, and ^2H solid-state (wide-line and MAS) NMR spectroscopy. Material **1** is shown to be unusual because 1) few nanoporous materials exhibit a well-organised 3D framework of water molecules, 2) it provides a unique opportunity to follow experimentally and to rationalise the deconstruction of a 3D water framework and 3) despite the fact that the hybrid framework is a supramolecular salt, the structure does not collapse after dehydration and the final material is crystalline.

Keywords: hybrid materials · hydrogen bonds · ice framework · supramolecular chemistry · water chemistry · X-ray diffraction

Introduction

Water, the basis of life, plays an important role in many biological and chemical systems and also in atmospheric chemistry.[1] Remarkably, it may self-assemble into nanoclusters, which are discrete hydrogen-bonded assemblies of molecules of water, rather than as an isotropic collection. The study of these individual clusters in confined spaces has received increasing attention in recent years due to various widespread improved techniques for treating hydrogen-bonded systems. Indeed, the exploration of the structural and binding properties of small water clusters provides a key for understanding bulk water, either in its liquid or solid phase, and also provides insight into the solvation phenomena.[2]

Pores, channels, and cavities of microporous organic–inorganic hybrid materials are ideal containers for studying the nature and behaviour of water clusters. In particular, interest in water clusters confined in metal–organic frameworks (MOF), structures and related materials is very recent, and emerged, for example, from the description by Barbour et al. of an intermolecular decameric cluster encapsulated in a supramolecular organic–inorganic matrix.[3] Many different water clusters have been characterised in a variety of MOFs and related materials:[4] dimers, tetramers, pentamers, hexamers, octamers, decamers, dodecamers, tetradecamers, hexadecamers, octadecamers, and others.

Here, we wish to describe a supramolecular salt, $[H_2pip]_3[Ge(hedp)_2]\cdot 14H_2O$ (**1**) [H_2pip^{2+} = piperazine cation $C_4H_{12}N_2^{2+}$; $hedp^{5-}$ = deprotonated form of etidronic acid, $C_2H_3P_2O_7^{5-}$), consisting of an organic–inorganic hybrid, hydrogen-bonded, nanoporous framework, embedding a rare 3D assembly of hydrogen-bonded water molecules. This "ice" scaffold is constructed from three different water nanoclusters, with distinct hydrogen-bonding strengths, templated by the hybrid framework. Above ≈0 °C, the water molecules become increasingly mobile and disordered. Intriguingly, the "ice" framework is stable up to ≈22 °C (TGA), and its deconstruction occurs in a stepwise fashion

[a] Prof. Dr. J. Rocha, Dr. F.-N. Shi, Dr. F. A. A. Paz, Dr. L. Mafra, Dr. M. Sardo, Dr. L. Cunha-Silva, Prof. Dr. P. Ribeiro-Claro, Prof. Dr. T. Trindade
Department of Chemistry, CICECO
University of Aveiro, 3810-193 Aveiro (Portugal)
Fax: (+351) 234-370084
E-mail: rocha@ua.pt

[b] Dr. J. Chisholm
Cambridge Crystallographic Data Centre
12 Union Road, Cambridge, CB2 1EZ (UK)

Supporting information for this article is available on the WWW under http://dx.doi.org/10.1002/chem.201000431.

 © 2010 Wiley-VCH Verlag GmbH & Co. KGaA, Weinheim

from 3D to 2D and discrete water aggregates (0D). In the process, however, the long-range order of the hybrid host is preserved.

Results and Discussion

Crystal structure: The crystal structures of the hydrated hybrid salt **1**, determined at 100, 200 and 295 K (see Experimental Section), show that this compound is stable over a wide range of temperatures, with no significant structural changes being observed up to ≈295 K. Indeed, the low-temperature structure differs from the room temperature one by, mainly, positional disorder for some water molecules. The structure of **1** is remarkable because it consists of two independent hydrogen-bonded interwoven frameworks, in which one is a hybrid and the other one is built up of water molecules only (Figures 1–3, and Figures S1 and S2 in the Supporting Information).

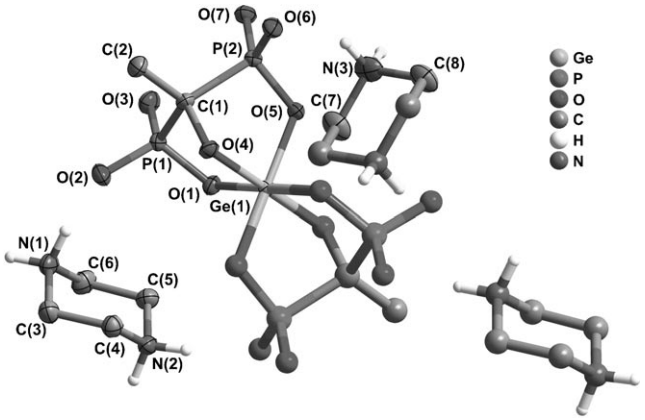

Figure 1. Mixed ellipsoid and ball-and-stick representation of the centrosymmetric hybrid compound $[H_2pip]_3[Ge(hedp)_2]\cdot 14H_2O$, showing the atom labelling for non-hydrogen atoms composing the asymmetric unit, which are represented with thermal ellipsoids drawn at the 80% probability level. Water molecules of crystallization and most of the hydrogen atoms are omitted for clarity (only the protonating hydrogen atoms of the pyperazinium cations are represented).

The hybrid framework is assembled by a centrosymmetric $[Ge(hedp)_2]^{6-}$ ion and two crystallographically independent (and centrosymmetric) H_2pip^{2+} ions (Figure 1), which play distinct roles: whereas the anion has an entourage of oxygen atoms acting as acceptors in hydrogen-bonding networks, the cations are the donors. One type of H_2pip^{2+} ion encloses the anion, with all the strong and highly directional N^+–$H\cdots O^-$ bonds leading to the formation of a layer in the *bc* plane. The second kind of H_2pip^{2+} ion acts as a pillar between the layers (along [100]) through a single N^+–$H\cdots O^-$ bond. The result is a porous framework with ≈36% accessible volume, which is occupied by structurally organised water molecules (Figures 2 and 3), seven of which are crystallographically independent.

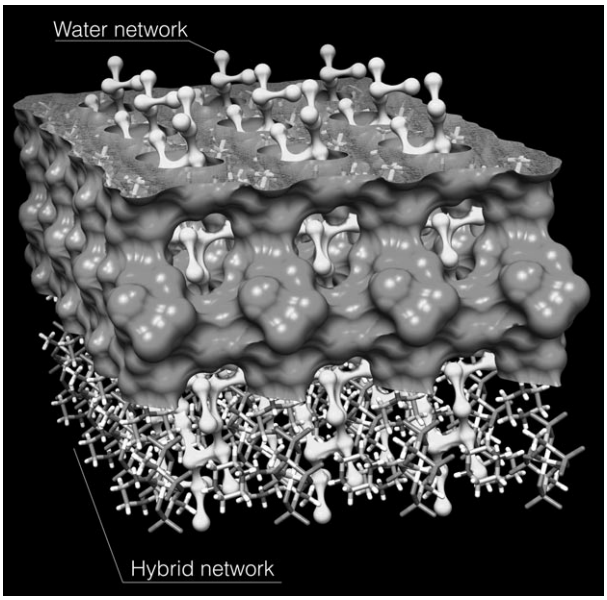

Figure 2. Representation of the interwoven nature of the water and hybrid networks present in **1**.

Whereas the internal surface of this hybrid framework is rich in hydrogen-bonding acceptors (O atoms of the anions), the pillaring H_2pip^{2+} ion has one free N^+–H able to establish connections with water molecules. As a consequence, the distribution of the water molecules within the voids is not random: their anchoring sites determine the strength of the water-to-water hydrogen bonds which, in general, are strong (d(D···A) < 2.9 Å) and highly directional ($\sphericalangle$(DHA) > 150°), as revealed by a metric study of the crystal structure at 100 K (Table 1). The shorter connections involve O(3W) and O(4W), and the disordered O(6W/7W) water molecules (range 2.732(11)–2.766(2) Å) form a linear hexamer (green "brick", Figure 4); O(5W) and the disordered O(8W)/O(9W) (range 2.764(3)–2.783(4) Å) create hydrogen-bonded dimers (red "brick", Figure 4), which are, in turn, connected to the aforementioned hexamers through weaker linking interactions (range 2.790(2)–3.276(10) Å), forming a water decamer. It is worth noting that the decamers are cross-linked through O(5W)···O(5W) hydrogen bonds (d(D···A) = 2.836(2) Å) along the [010] direction of the unit cell to form a water layer (Figure 4, top right). A 3D water network is ultimately achieved through O(1W) water dimers (d(D···A) = 2.801(2) Å) connected to the individual decamers at the O(5W) binding site (Figure 4, bottom left). The interpenetration of 3D water and hybrid networks is a rare structural feature, as evidenced by an in-depth search of the Cambridge Structural Database.

Above 200 K the structural integrity of the single crystals under the X-ray beam is limited. Nevertheless, crystallographic studies clearly revealed that the overall structural features described above are retained up to ambient temperature (Tables 2 and 3), with only the disorder features of O(6W/7W) and O(8W/9W) disappearing.

 © 2010 Wiley-VCH Verlag GmbH & Co. KGaA, Weinheim

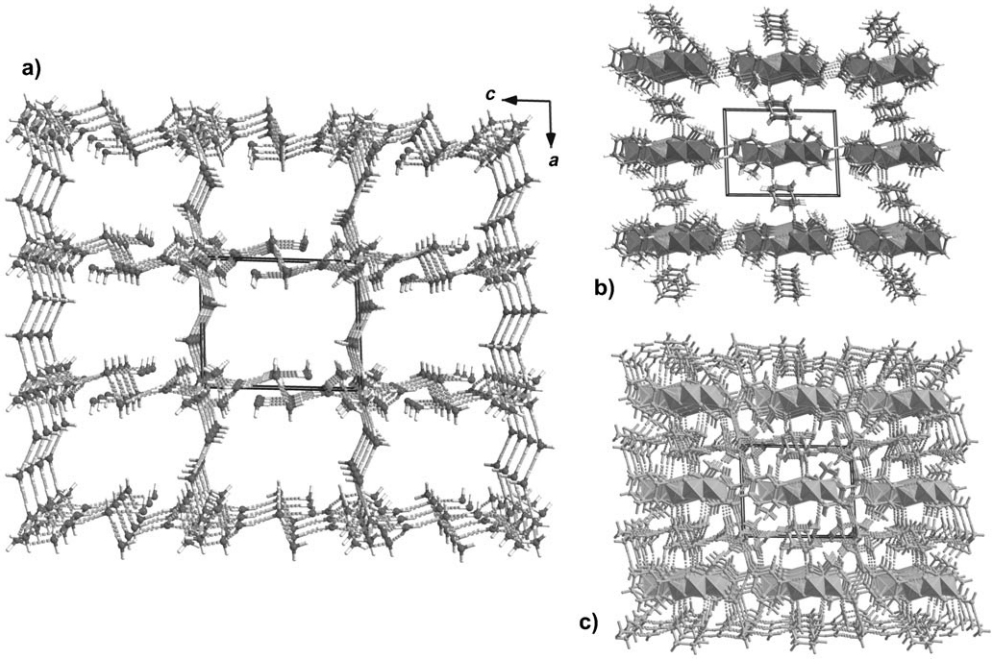

Figure 3. Perspective views along the [010] direction of the unit cell of the 3D hydrogen-bonded interwoven frameworks: a) water framework; b) hybrid framework; and c) interpenetration of the frameworks.

Thermogravimetry: Thermogravimetric analysis reveals that the water framework of deuterated **1** is disrupted in a complex process, in three major steps, up to ≈120 °C. At a 2 °C min^{-1} (air) heating rate, these three thermal events take place at: ≈22–50 °C −9.4 %; ≈51–88 °C −6.0 %; ≈89–120 °C −11.1 % (Figure 5).

Considering the structural features described above, it is feasible to assume that the first two weight losses corre-

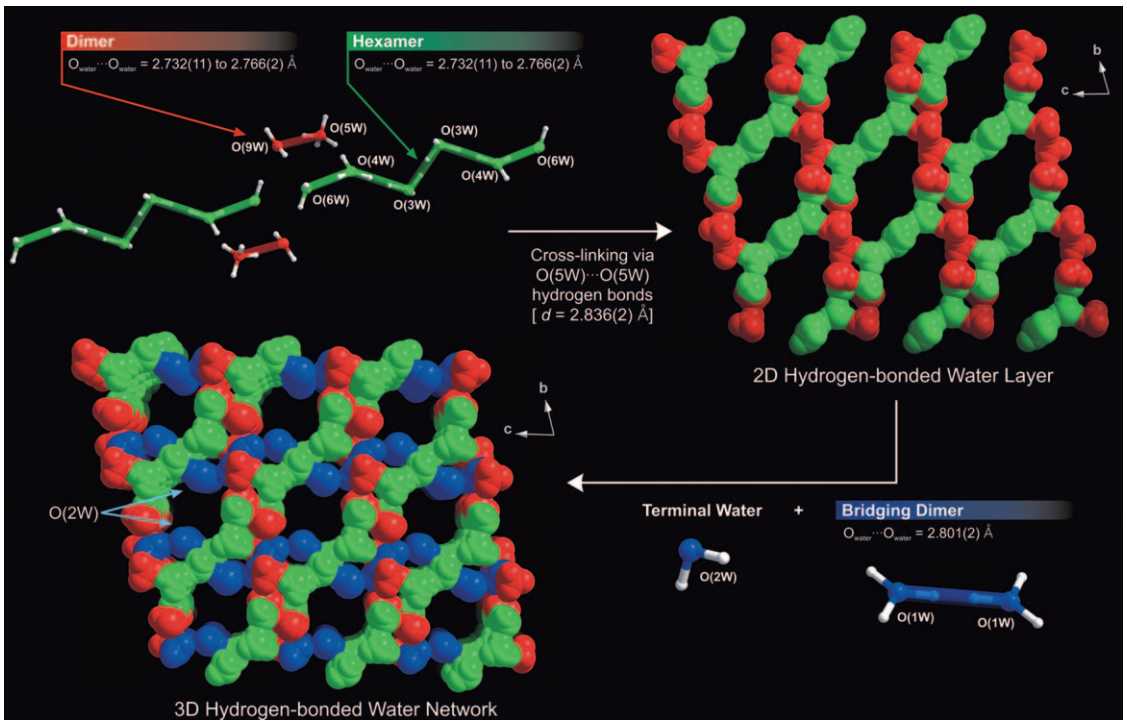

Figure 4. Construction of the 3D hydrogen-bonded water network through the self-assembly of three distinct hydrogen-bonded units based on the strength of the interactions. For simplicity only one position of the disordered water molecules is represented.

 © 2010 Wiley-VCH Verlag GmbH & Co. KGaA, Weinheim

Table 1. Hydrogen bonding geometry found in the crystal structure of $[H_2pip]_3[Ge(hedp)_2]\cdot 14H_2O$ at 100 K.[a]

D–H···A	d(H···A) [Å]	d(D···A) [Å]	∢(DHA) [°]
N(1)–H(1A)···O(2)	1.808(4)	2.6923(17)	167.1(17)
N(1)–H(1B)···O(3)^{ii}	1.7754(19)	2.6751(17)	178.3(14)
N(2)–H(2D)···O(6)^{i}	1.749(2)	2.6440(17)	172.4(13)
N(2)–H(2E)···O(7)^{iii}	1.890(3)	2.7796(17)	169.2(13)
N(3)–H(3C)···O(4)^{iv}	1.751(8)	2.6053(17)	157.4(19)
N(3)–H(3D)···O(2W)^{i}	1.838(6)	2.7140(19)	164(2)
O(1W)–H(1C)···O(3)^{i}	2.472(17)	3.0684(17)	124.1(16)
O(1W)–H(1C)···O(7)^{i}	2.045(11)	2.8439(16)	147.3(18)
O(1W)–H(1D)···O(5W)^{v}	1.935(3)	2.8319(19)	175(2)
O(1W)–H(1E)···O(1W)^{vi}	1.901(3)	2.801(2)	179(5)
O(2W)–H(2F)···O(7)^{i}	1.783(3)	2.6763(17)	171.7(17)
O(2W)–H(2G)···O(3W)	1.920(2)	2.8194(18)	177.5(18)
O(3W)–H(3E)···O(6)^{iii}	1.821(3)	2.7131(17)	170.8(18)
O(3W)–H(3F)···O(4W)	1.872(5)	2.765(2)	171(2)
O(3W)–H(3G)···O(3W)^{vii}	1.877(4)	2.766(2)	169.1(18)
O(4W)–H(4C)···O(6W)^{viii}	1.871(8)	2.748(4)	164(2)
O(4W)–H(4C)···O(7W)^{viii}	1.843(12)	2.732(11)	169(3)
O(4W)–H(4D)···O(3W)	1.893(10)	2.765(2)	163(3)
O(4W)–H(4E)···O(5W)	1.910(14)	2.790(2)	165(5)
O(5W)–H(5C)···O(8W)^{ix}	1.891(5)	2.783(4)	171(2)
O(5W)–H(5C)···O(9W)^{ix}	1.898(8)	2.764(3)	160.6(19)
O(5W)–H(5D)···O(4W)	1.949(10)	2.790(2)	155(2)
O(5W)–H(5E)···O(5W)^{x}	1.940(4)	2.836(2)	173(2)
O(5W)–H(5F)···O(1W)^{xi}	1.942(5)	2.8319(19)	170(2)
O(6W)–H(6C)···O(3)	1.810(2)	2.702(3)	171.0(18)
O(6W)–H(6D)···O(8W)^{iv}	1.906(6)	2.802(5)	173.1(19)
O(6W)–H(7D)···O(9W)^{iv}	1.985(4)	2.871(4)	168.0(17)
O(7W)–H(7C)···O(3)	1.810(2)	2.664(9)	157.7(19)
O(7W)–H(7D)···O(8W)^{iv}	1.906(6)	2.672(9)	141.8(19)
O(7W)–H(7D)···O(9W)^{iv}	1.985(4)	2.840(9)	158.2(19)
O(8W)–H(8C)···O(2)	1.888(3)	2.783(4)	172.6(9)
O(8W)–H(8D)···O(5W)^{ix}	1.890(8)	2.783(4)	171(4)
O(9W)–H(8C)···O(2)	1.888(3)	2.684(3)	146.5(7)
O(9W)–H(9B)···O(6W)^{ii}	1.992(7)	2.807(3)	149.9(11)
O(9W)–H(9B)···O(7W)^{ii}	2.464(11)	3.276(10)	150.2(9)

[a] Symmetry transformations used to generate equivalent atoms: i: $-x+1, -y+1, -z+1$; ii: $-x+1, -y+1, -z$; iii: $x, y-1, z$; iv: $x+1, y, z$; v: $x, y, z+1$; vi: $-x+1, -y, -z+2$; vii: $-x, -y, -z+1$; viii: $-x+1, y, z$; ix: $-x, -y+1, -z$; x: $-x, -y, -z$; xi: $x, y, z-1$.

Table 2. Hydrogen bonding geometry found in the crystal structure of $[H_2pip]_3[Ge(hedp)_2]\cdot 14H_2O$ at 200 K.[a]

D–H···A	d(H···A) [Å]	d(D···A) [Å]	∢(DHA) [°]
N(1)–H(1A)···O(2)^{i}	1.801(5)	2.692(2)	170(3)
N(1)–H(1B)···O(3)^{ii}	1.799(5)	2.691(2)	170(3)
N(2)–H(2D)···O(6)^{iii}	1.753(4)	2.645(2)	171(2)
N(2)–H(2E)···O(7)	1.893(5)	2.780(2)	168.1(19)
N(3)–H(3C)···O(4)	1.743(10)	2.617(2)	163(3)
N(3)–H(3D)···O(2W)^{iv}	1.828(8)	2.713(3)	167(3)

[a] Symmetry transformations used to generate equivalent atoms: i: $x, y+1, z$; ii: $-x+1, -y+1, -z$; iii: $-x+1, -y+1, -z+1$; iv: $x-1, y, z$.

Table 3. Hydrogen-bonding geometry found in the crystal structure of $[H_2pip]_3[Ge(hedp)_2]\cdot 14H_2O$ at 295 K.[a]

D–H···A	d(H···A) [Å]	d(D···A) [Å]	∢(DHA) [°]
N(1)–H(1A)···O(2)^{i}	1.790(6)	2.684(6)	172(3)
N(1)–H(1B)···O(3)^{ii}	1.811(6)	2.707(6)	173(3)
N(2)–H(2D)···O(6)^{iii}	1.748(6)	2.641(6)	171(3)
N(2)–H(2E)···O(7)	1.875(9)	2.761(8)	168(3)
N(3)–H(3C)···O(4)^{iv}	1.767(16)	2.623(6)	158(4)
N(3)–H(3D)···O(2W)	1.829(8)	2.725(7)	174(4)

[a] Symmetry transformations used to generate equivalent atoms: i: $x, y+1, z$; ii: $-x, -y+1, -z$; iii: $-x, -y+1, -z+1$; iv: $x+1, y, z$.

spond to the consecutive release of the more weakly bonded water molecules, starting with the terminal O(2W) water and the bridging O(1W) dimers, and finishing with the dimer of the decamers. The water molecules that are more strongly hydrogen bonded, that is, those of the hexameric units, are assumed to be the last to be released. Hence, this transformation is parallel to a 3D→2D→0D transformation of the dimensionality of the network of hydrogen bonds (Figure 4 in reverse order). A notable point to emphasise concerns the fact that the crystallinity of the compound is never disrupted, as shown by variable-temperature powder X-ray diffraction studies (Figure 6). Additionally, at 150 °C

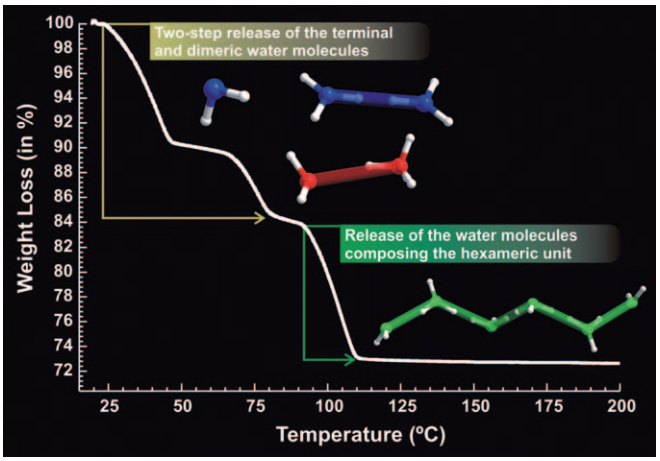

Figure 5. Thermogravimetric analysis and weight loss attribution of deuterated **1**. Experimental conditions: Shimadzu TGA 50, with a heating rate of 2 °C min^{-1} from room temperature to 200 °C, under a continuous flow of air with a rate of 20 cm^3 min^{-1}.

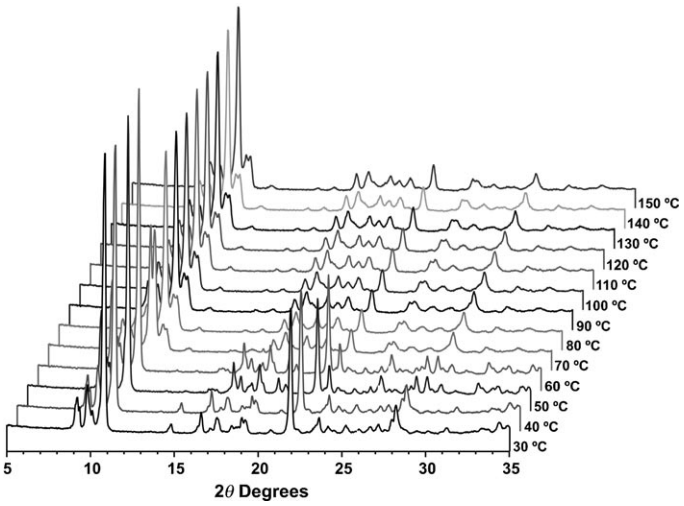

Figure 6. Variable-temperature powder X-ray diffraction data showing the thermal stability of **1** up to ≈150 °C, and its transformation into the respective dehydrated crystalline phase. Phase identification of the in situ generated phase at 150 °C through a Le Bail whole-powder-diffraction-pattern profile fitting is provided as Figure S3.

© 2010 Wiley-VCH Verlag GmbH & Co. KGaA, Weinheim

the residue is crystalline, and was indexed with the related, but smaller, unit cell parameters of **1**@295 K (Figure S3 in the Supporting Information), thus supporting a seamless release of water molecules with parallel ordering of the hybrid network.

Solid-state NMR spectroscopy: To gain insight into the nature of the molecular dynamics of the water framework, wide-line (static) ^{2}H NMR spectra of deuterated samples were recorded at 192–363 K. The static quadrupole-powder patterns are sensitive to motions with frequency 10^4–10^7 Hz, making ^{2}H NMR an ideal tool for studying molecular dynamics in solids. Figures 7 and S4 (Supporting Information)

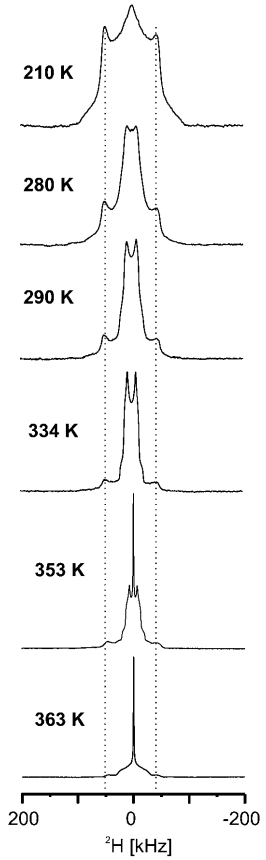

Figure 7. Selected ^{2}H NMR spectra of **1** recorded at 210–363 K. Dashed lines depict the main features of the quadrupolar splitting (Pake doublet) attributed to deuterons in the rigid organic matrix of the framework. The relatively sharp, inner, Pake doublet is assigned to the water molecules in the octameric units.

show selected ^{2}H quadrupole-echo NMR spectra of **1** recorded at different temperatures. Up to ≈270 K the spectra consist of a broad Pake pattern, attributed to ND_2 sites of the piperazine rings of the hybrid framework, and a relatively sharp peak assigned to the more mobile water molecules. This attribution is in accord with the assignment proposed in a previous study on a pharmaceutical crystalline hydrate.[5] To further pursue this assignment, ^{2}H MAS NMR spectra (Figure 8) were recorded (at room temperature), and they

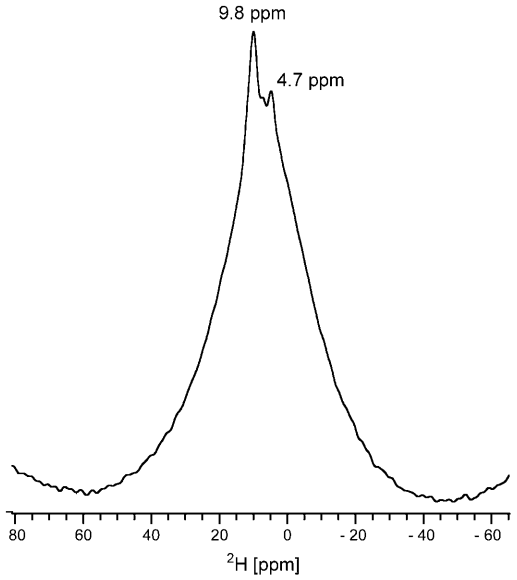

Figure 8. ^{2}H MAS NMR spectrum recorded at room temperature, 296 K ($\upsilon_R = 8$ kHz).

clearly show the presence of two main ^{2}H chemical environments: 1) a peak at 4.7 ppm, superimposed on a broader resonance centred at 5–6 ppm, attributed to water, and 2) a second peak at 9.8 ppm, assigned to the ND_2 species of the piperazine rings. This is in excellent agreement with the assignment proposed in reference [2]. The sharp peak at 4.7 ppm is probably due to some free water liberated upon MAS, and the concomitant temperature rise (note that deuterated water resonates at 4.7 ppm).

At 280 K, and up to 353 K, the broad doublet is still present, but the sharp peak is replaced by a narrow Pake doublet with an effective quadrupolar splitting $\delta_{Q,eff} = 18$ kHz (≈11 % of the unaveraged δ_Q value, 165 kHz, fast motion limit $\tau_C \ll \delta_Q^{-1}$ (τ_C is the motion correlation time)).

We now discuss in detail the 280–354 K spectra, focusing our attention on the narrow Pake doublet attributed to the water molecule framework. Although the full picture is likely to be more complex (e.g., the resolution of the doublet singularities improves with temperature, but this is not considered here), essentially, these molecules undergo a complex jump between two sites with non-equal populations. Figure 9 shows four possible models for a two-site 180° jump process on a cone. An acceptable simulation of the water Pake doublet requires a Gaussian distribution of jump angles between the two deuteron sites (Figure 9c and 9d). Assuming such a distribution, the line shape is narrowed by a factor of approximately five (relative to the undistributed case, Figure 9a and 9b), resulting in $\delta_{Q,eff} =$ 18 kHz (Figure 9d and 9e). The very large jump-angle distribution ($2\sigma = 110°$) required to simulate the Pake doublet indicates that the water molecules are disordered in the structure. Simulation of the water Pake doublet also affords a non-zero effective asymmetry parameter ($\eta_{Q,eff} \approx 0.3$), indicating some departure from the axial symmetry. Among the

 © 2010 Wiley-VCH Verlag GmbH & Co. KGaA, Weinheim

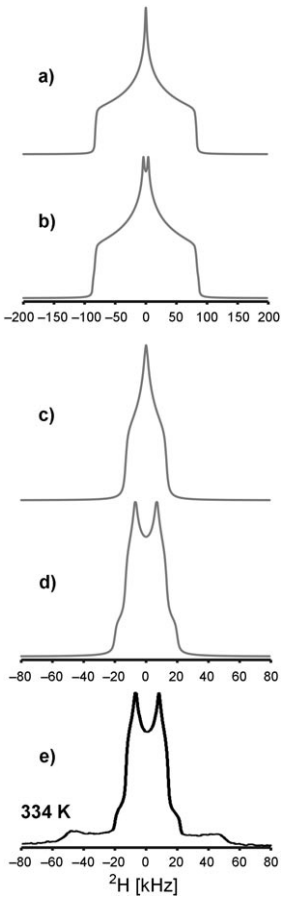

Figure 9. Simulated (a–d) and experimental (e) quadrupole-echo ^{2}H NMR spectra. a,b) spectra simulated assuming discrete jumps (angle $\phi = 180°$) between two sites with equal ($p1 = p2 = 0.5$) and non-equal ($p1 = 0.43$, $p2 = 0.57$) populations. c,d) spectra simulated using a two-site jump ($\phi = 180°$) with populations, respectively, $p1 = p2 = 0.5$ and $p1 = 0.43$, $p2 = 0.57$, with a Gaussian jump-angle distribution full width $2\sigma = 110°$. A half-cone angle $\theta = 54.7°$ and a 2 kHz Lorentzian broadening were used in all simulations. Simulated line shapes are for the fast motion limit. The motional unaveraged anisotropy parameter $\delta_Q = 3/4 \times C_Q$ (kHz) and the asymmetry parameter, η_Q, of the electric field gradient tensor were set to 165 kHz (equivalent to $C_Q = 220$ kHz in rigid water) and 0 (axial symmetry), respectively.

various possible reasons for this, a two-site non-equal population jump on a cone is the most likely one.

Below 280 K, the water peak loses intensity relative to the broad Pake doublet (Figure 7). This may be due to destructive interference during refocusing, which occurs when the rate of the re-orientation dynamics is comparable to $\delta_Q \approx 10^5$ Hz (intermediate motion regime). Moreover, in ^{2}H quadrupolar-echo experiments, the signal is lost during the echo delays in different amounts for the two components, due to differences in transverse relaxation. At 363 K and above, the extreme narrowing of the central line reveals that the water molecules are undergoing isotropic re-orientation with a rate $> 10^6$ Hz. Heating the sample for a few minutes at 363 K leads to the complete removal of water, and the disappearance of the sharp Pake doublet (not shown).

Raman spectroscopy study of H/D isotopic substitution: The dynamics of the water structure is also revealed by monitoring the H/D isotopic substitution (promoted by exposure of the sample crystalline powder to conditions of 100% D_2O relative humidity[6]) through the νOH/νOD Raman stretching band. The H/D exchange (deuteration) in **1** is about twice as fast as the reverse process (D/H), indicating that the rate-determining step for the H/D substitution mechanism is not the cleavage of the O–H and O–D bonds (in such a case the observed ratio would be ≈ 10). The mechanism is most probably controlled by the diffusion of D_2O/H_2O molecules within the crystal.[6]

The analysis of the spectra as a function of the time of exposure to the D_2O atmosphere reveals OH/D oscillators with different exchange rates.

The presence of a low-intensity νOD band is observed within the first half hour of exposure (Figure 10, lower trace). Because the band profile closely resembles that of

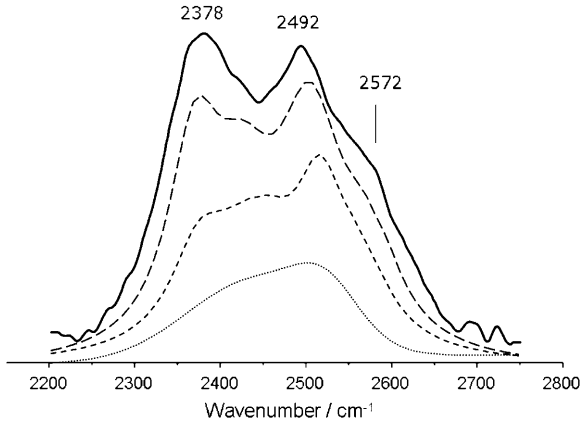

Figure 10. Raman spectra of deuterated **1** in the region of the νOD stretching modes, after exposure to a D_2O atmosphere. Times of exposure from bottom to top: 30 min, 6 h, 22 h, and 7 days.

bulk heavy water, it is ascribed to "unstructured" D_2O molecules adsorbed in the sample. After this initiation period, three main steps (corresponding to different types of "structured" D_2O molecules) are identified.

The first step is observed within the first 6 h, and corresponds to the definition of a νOD band profile with its maximum intensity at ≈ 2520 cm^{-1} and lower intensity components at ≈ 2442 and 2378 cm^{-1}. The second step occurs between 6–10 h, leading to the intensification of the peak at ≈ 2378 cm^{-1}. In this period a shoulder appears at ≈ 2572 cm^{-1}. The third step leads to the final νOD profile (Figure 10, top trace), in which the shoulder at ≈ 2572 cm^{-1} is clearly defined and the band at ≈ 2378 cm^{-1} becomes the most intense one. This behaviour is compatible with the presence of three different water sites with different exchange dynamics.

 © 2010 Wiley-VCH Verlag GmbH & Co. KGaA, Weinheim

Conclusion

In conclusion, the supramolecular salt $[H_2pip]_3[Ge(hedp)_2]\cdot 14H_2O$ features a rare 3D assembly of hydrogen-bonded water molecules embedded in a hybrid matrix. The deconstruction of the "ice" framework begins at ≈22 °C, occurring in a stepwise fashion from 3D to 2D to 0D, while the long-range order of the hybrid host is preserved.

Experimental Section

Synthesis of $[H_2pip]_3[Ge(hedp)_2]\cdot 14H_2O$ (1): A suspension containing 1-hydroxyethylidenediphosphonic acid (0.20 g) (H_5hedp, $C_2H_8O_7P_2$, ≥97%, Fluka), germanium(IV) oxide amorphous (0.10 g) (GeO_2, 99.99%, Aldrich), and piperazine anhydrous (0.140 g) (pip, $C_4H_{10}N_2$, 98%, Merck) in distilled water (≈15 g or 15 g of deuterium oxide, D_2O, 99.996%, Aldrich, for the synthesis of the deuterated analogue) was stirred for 30 min at ambient temperature. The reactive mixture was transferred to a PTFE-lined stainless steel reaction vessel (≈40 cm^3) and placed inside an oven. The temperature was gradually increased from ambient temperature to 393 K and kept constant for three days, after which the vessel was allowed to cool slowly to ambient temperature before opening. The resulting block colourless crystals were obtained by evaporation of the clear colourless mother liquid for three days, washed with a small amount of distilled water (or D_2O), filtered and air-dried at ambient temperature, yielding ≈21.1% or 19.8%, based on H_5hedp, for **1** or its deuterated analogue, respectively. Elemental analysis calcd (%) (based on single-crystal data): C 19.37, N 8.47, H 7.06; found: C 19.03, N 7.97, H 6.21.

Single-crystal X-ray diffraction studies: Suitable single crystals of $[H_2pip]_3[Ge(hedp)_2]\cdot 14H_2O$ **(1)** were manually harvested from the crystallization vials and mounted on Hampton Research CryoLoops or thin glass fibres using FOMBLIN Y perfluoropolyether vacuum oil (LVAC 25/6, purchased from Aldrich) with the help of a Stemi 2000 stereomicroscope equipped with Carl Zeiss lenses.[7] Complete single-crystal data sets were collected at 100(2) (**1**@100 K), 200(2) (**1**@200 K) and 295(2) K (**1**@295 K), on a Bruker X8 Kappa APEX II charge-coupled device (CCD) area-detector diffractometer ($Mo_{K\alpha}$ graphite-monochromated radiation, $\lambda = 0.71073$ Å), controlled by the APEX-2 software package,[8] and equipped with an Oxford Cryosystems Series 700 cryostream monitored remotely using the software interface Cryopad. Additional short data sets (3 runs of 12 images each) were performed at several temperatures ranging between 90(2) and 240(2) K with steps of ≈10 K, in order to establish the unit cell parameter trends in this temperature range (data not shown). Images were processed using the software package SAINT+,[9] and data were corrected for absorption by the multi-scan semi-empirical method implemented in SADABS.[10] Structures were solved using the direct methods implemented in SHELXS-97,[11] which allowed the immediate location of the majority of the heaviest atoms. All the remaining non-hydrogen atoms were directly located from difference Fourier maps calculated from successive full-matrix least-squares refinement cycles on F^2 using SHELXL-97.[11a,12] Non-hydrogen atoms of all materials were successfully refined using anisotropic displacement parameters.

In all three structures the hydrogen atoms bound to carbon were located at their idealized positions using appropriate HFIX instructions in SHELXL (137 for the $-CH_3$ group of the $hedp^{5-}$ ligand and 23 for the $-CH_2-$ moieties of the diprotonated piperazine cations), and included in subsequent refinement cycles in riding-motion approximation with isotropic thermal displacement parameters (U_{iso}) fixed at 1.5 and 1.2 times U_{eq} of the carbon atom to which they are attached for the $-CH_3$ and $-CH_2-$ groups, respectively. Hydrogen atoms associated with the nitrogen atoms of the diprotonated piperazine cations (NH_2) were markedly visible in difference Fourier maps, and were included in the structure with the N–H and H···H distances restrained to 0.90(1) and 1.47(1) Å, respectively (in order to ensure a chemically reasonable geometry for these molecules), and with $U_{iso} = 1.5 \times U_{eq}$(N). In the **1**@100 K structure, the hydrogen atoms associated with the crystallization water molecules (uncoordinated molecules) were directly located from difference Fourier maps. These hydrogen atoms were included in the final structural models with the O–H and H···H distances restrained to 0.90(1) and 1.47(1) Å, respectively (ensuring a chemically reasonable geometry for these molecules), and by assuming a riding-motion approximation with an isotropic thermal displacement parameter fixed at $1.5 \times U_{eq}$ of the oxygen atom to which they are attached. In the remaining **1**@200 K and **1**@295 K structures the hydrogen atoms associated with the crystallization water molecules were not included in the structure, but were considered for the final molecular formulae.

The last difference Fourier map synthesis showed (Table 4): for **1**@100 K, the highest peak (0.50 e $Å^{-3}$) and deepest hole (−0.37 e $Å^{-3}$) located at 0.74 Å from C(6) and 0.41 Å from P(2), respectively; for **1**@200 K, the highest peak (0.86 e $Å^{-3}$) and deepest hole (−0.59 e $Å^{-3}$) located at 0.79 Å and 0.78 Å from O(7W), respectively; for **1**@295 K, the highest peak (0.78 e $Å^{-3}$) and deepest hole (−0.85 e $Å^{-3}$) located at 1.21 Å and 0.41 Å from O(2W), respectively.

Variable-temperature powder X-ray diffraction: Variable-temperature powder X-ray diffraction data were collected on an X′Pert MPD Philips diffractometer ($Cu_{K\alpha}$ X-radiation, $\lambda = 1.54060$ Å), equipped with an X′Celerator detector, curved graphite-monochromated radiation, a flat-plate sample holder in a Bragg–Brentano para-focusing optics configuration (40 kV, 50 mA), and a high-temperature Antoon Parr HKL 16 chamber controlled by an Antoon Parr 100 TCU unit. Intensity data were collected in step mode (0.03°, 2 s per step) in the range $\approx 5 \leq 2\theta \leq 35°$. Data were collected between 30 °C and 150 °C at intervals of 10 °C.

CCDC-720123 (**1**@100 K), 720124 (**1**@200 K) and 720125 (**1**@295 K) contain the supplementary crystallographic data for this paper. These data can be obtained free of charge from The Cambridge Crystallographic Data Centre via www.ccdc.cam.ac.uk/data_request/cif.

Le Bail whole-powder-diffraction-pattern profile fitting of the phase at 150 °C: Conventional powder X-ray diffraction data were collected at ambient temperature on an X′Pert MPD Philips diffractometer ($Cu_{K\alpha 1,2}$ X-radiation, $\lambda_1 = 1.540598$ Å, and $\lambda_2 = 1.544426$ Å), equipped with an X′Celerator detector, curved graphite-monochromated radiation, and a flat-plate sample holder in a Bragg–Brentano para-focusing optics configuration (40 kV, 50 mA). Intensity data were collected by the step-counting method (step 0.03°), in continuous mode, in the $5 \leq 2\theta \leq 50°$ range.

The experimental powder X-ray diffraction pattern of the compound obtained from calcination at 150 °C was indexed with DICVOL04,[13] and by employing the first 18 well-resolved reflections (located using the derivative-based peak search algorithm provided with Fullprof.2k)[14] and a fixed absolute error on each line of 0.03° 2θ. Initial unit cell metrics were obtained with reasonable figures-of-merit. Analysis of the systematic absences was performed using CHECKCELL.[15]

A Le Bail whole-powder-diffraction-pattern profile fitting was performed with FullProf.2k[14] by applying fixed background points throughout the entire angular range determined by the linear interpolation between consecutive (and manually selected) breakpoints in the powder pattern. Pseudo-Voigt profile functions were selected to generate the line shapes of the simulated diffraction peaks. The angular dependence of the full-width-at-half-maximum (FWHM) of individual reflections was also taken into account by employing a Caglioti function correction.[16] Zero shift, scale factor, parameters related to peak shape, and unit cell parameters were consecutively added as fully refinable variables upon previous full convergence of the remaining parameters to their optimal values. The corresponding final plot is supplied in Figure S3 (Supporting Information).

Solid-state NMR: ^2H NMR spectra were recorded at 61.4 MHz (9.4 T) on a Bruker Avance spectrometer, using a standard 5 mm high-power static probe and a quadrupole-echo pulse sequence, $(\pi/2)x-\tau_1-(\pi/2)y-\tau_2-$acq, with $\pi/2 = 5$ μs, $\tau_1 = \tau_2 = 20$ μs, and a 2 s recycle delay. The temperature range studied was 191–363 K. At each temperature, 30 minutes were allowed for thermal equilibration prior to NMR measurements. The programme Weblab (v4.1.2),[17] was used for ^2H line shape

 © 2010 Wiley-VCH Verlag GmbH & Co. KGaA, Weinheim

Table 4. Crystal and structure refinement data for $[H_2pip]_3[Ge(hedp)_2]\cdot 14\,H_2O$ collected at 100, 200 and 295 K.

	1@100 K	**1**@200 K	**1**@295 K
formula	$C_{16}H_{70}GeN_6O_{28}P_4$	$C_{16}H_{70}GeN_6O_{28}P_4$	$C_{16}H_{70}GeN_6O_{28}P_4$
M_r	991.25	991.25	991.25
T	100(2)	200(2)	295(2)
crystal system	triclinic	triclinic	triclinic
space group	$P\bar{1}$	$P\bar{1}$	$P\bar{1}$
a [Å]	9.531(4)	9.5856(4)	9.61(2)
b [Å]	10.457(4)	10.4736(4)	10.41(3)
c [Å]	11.386(4)	11.4045(4)	11.41(2)
α [°]	75.090(17)	75.039(2)	74.92(3)
β [°]	87.802(19)	88.003(2)	88.33(3)
γ [°]	70.612(17)	70.870(2)	71.39(3)
V [Å^3]	1033.0(7)	1043.51(7)	1043(4)
Z	1	1	1
ρ_{calcd} [g cm^{-3}]	1.593	1.577	1.579
μ ($Mo_{K\alpha}$) [mm^{-1}]	0.995	0.985	0.985
F(000)	524	524	524
crystal size [mm]	$0.45\times0.45\times0.35$	$0.35\times0.35\times0.30$	$0.45\times0.35\times0.28$
crystal type	colourless blocks	colourless blocks	colourless blocks
θ range [°]	3.60–29.13	3.58–30.03	3.68–29.13
index ranges	$-12\le h\le 13$	$-13\le h\le 13$	$-12\le h\le 13$
	$-14\le k\le 14$	$-14\le k\le 14$	$-14\le k\le 14$
	$-15\le l\le 15$	$-16\le l\le 16$	$-15\le l\le 15$
reflections collected	19598	79739	11104
independent reflections	5494 ($R_{int}=0.0208$)	6069 ($R_{int}=0.0493$)	5381 ($R_{int}=0.0446$)
data completeness	to $\theta=29.13°$	to $\theta=30.03°$	to $\theta=29.13°$
	99.1 %	99.4 %	96.0 %
final R indices $[I>2\sigma(I)]$[a,b]	$R1=0.0251$	$R1=0.0365$	$R1=0.0476$
	$wR2=0.0686$	$wR2=0.1010$	$wR2=0.1150$
final R indices (all data)[a,b]	$R1=0.0269$	$R1=0.0444$	$R1=0.0713$
	$wR2=0.0696$	$wR2=0.1061$	$wR2=0.1260$
weighting scheme[c]	$m=0.0383$	$m=0.0603$	$m=0.0601$
	$n=0.4832$	$n=0.9331$	$n=0.0$
largest diff. peak/hole [e Å^{-3}]	0.503/−0.367	0.856/−0.590	0.776/−0.849

[a] $R_1=\Sigma||F_o|-|F_c||/\Sigma|F_o|$. [b] $wR_2=\{\Sigma[w(F_o^2-F_c^2)^2]/\Sigma[w(F_o^2)^2]\}^{1/2}$. [c] $w=1/[\sigma(F_o^2)+(mP)^2+nP]$ in which $P=(F_o^2+2F_c^2)/3$.

analysis, assuming a two-site exchange cone model. The input parameters used in the simulation are given in the figure captions. ^{2}H MAS NMR spectra were recorded at room temperature, with an MAS rate of 8 kHz and a single excitation pulse length of 2 μs. ^{2}H chemical shifts are quoted in ppm from D_2O.

Acknowledgements

We thank the reviewers for their useful comments. We also acknowledge Fundação para a Ciência e a Tecnologia (FCT) for funding (PTDC/QUI/65805/2006) and the Fundo Social Europeu. The NMR spectrometers are part of the National NMR Network and were purchased in the framework of the National Programme for Scientific Re-equipment, contract REDE/1517/RMN/2005, with funds from POCI 2010 (FEDER) and FCT. Finally, we thank Prof. J. J. Cruz Pinto (Aveiro) for assistance with the TG measurements.

[1] a) G. Vali in *Biological Ice Nucleation and Its Applications* (Eds.: R. E. Lee, Jr., G. J. Warren, L. V. Gusta), American Phytopathological Society Press, St. Paul, **1995**, Chapter 1; b) P. Ball, *Chem. Rev.* **2008**, *108*, 74–108.
[2] R. Ludwig, *Angew. Chem.* **2001**, *113*, 1856–1876; *Angew. Chem. Int. Ed.* **2001**, *40*, 1808–1827.
[3] L. J. Barbour, G. W. Orr, J. L. Atwood, *Nature* **1998**, *393*, 671–673.
[4] a) M. S. Deshpande, A. S. Kumbhar, V. G. Puranik, K. Selvaraj, *Cryst. Growth Des.* **2006**, *6*, 743–748; b) M. H. Mir, L. Wang, M. W. Wong, J. J. Vittal, *Chem. Commun.* **2009**, 4539–4541; c) M. C. Das, S. K. Ghosh, E. C. Sanudo, P. K. Bharadwaj, *Dalton Trans.* **2009**, 1644–1658; d) R. Abuhmaiera, Y. H. Lan, A. M. Ako, G. E. Kostakis, A. Mavrandonakis, W. Klopper, R. Clerac, C. E. Anson, A. K. Powell, *CrystEngComm* **2009**, *11*, 1089–1096; e) L. Y. Wang, Y. Yang, K. Liu, B. L. Li, Y. Zhang, *Cryst. Growth Des.* **2008**, *8*, 3902–3904; f) C. Y. Sun, X. J. Zheng, W. J. Li, M. W. Wang, C. Y. Fang, *Z. Anorg. Allg. Chem.* **2008**, *634*, 2663–2669; g) M. H. Mir, J. J. Vittal, *Cryst. Growth Des.* **2008**, *8*, 1478–1480; h) Q. Y. Liu, Y. L. Wang, J. Zhao, L. Xu, *Eur. J. Inorg. Chem.* **2008**, 1157–1163; i) F. N. Dai, H. Y. He, D. F. Sun, *J. Am. Chem. Soc.* **2008**, *130*, 14064–14065; j) H. H. Song, B. Q. Ma, *CrystEngComm* **2007**, *9*, 625–627; k) M. H. Mir, J. J. Vittal, *Angew. Chem.* **2007**, *119*, 6029–6032; *Angew. Chem. Int. Ed.* **2007**, *46*, 5925–5928; l) S. C. Manna, E. Zangrando, J. Ribas, N. R. Chaudhuri, *Eur. J. Inorg. Chem.* **2007**, 4592–4595; m) D. K. Kumar, A. Das, P. Dastidar, *CrystEngComm* **2007**, *9*, 895–901; n) N. H. Hu, Z. G. Li, J. W. Xu, H. Q. Jia, J. J. Niu, *Cryst. Growth Des.* **2007**, *7*, 15–17; o) F. N. Shi, L. Cunha-Silva, R. A. S. Ferreira, L. Mafra, T. Trindade, L. D. Carlos, F. A. A. Paz, J. Rocha, *J. Am. Chem. Soc.* **2008**, *130*, 150–167.
[5] F. G. Vogt, J. Brum, L. M. Katrincic, A. Flach, J. M. Socha, R. M. Goodman, R. C. Haltiwanger, *Cryst. Growth Des.* **2006**, *6*, 2333–2354.
[6] A. M. Amado, P. J. A. Ribeiro-Claro, *J. Chem. Soc. Faraday Trans.* **1997**, *93*, 2387–2390.
[7] T. Kottke, D. Stalke, *J. Appl. Crystallogr.* **1993**, *26*, 615–619.
[8] APEX2, Data Collection Software Version 2.1-RC13, Bruker AXS, Delft, **2006**.
[9] SAINT+, Data Integration Engine v. 7.23a © **1997–2005**, Bruker AXS, Madison, Wisconsin.
[10] SADABS v.2.01, G. M. Sheldrick, Bruker/Siemens Area Detector Absorption Correction Program **1998**, Bruker AXS, Madison, Wisconsin.
[11] a) G. M. Sheldrick, *Acta Crystallogr. Sect. A* **2008**, *64*, 112–122; b) SHELXS-97, Program for Crystal Structure Solution, G. M. Sheldrick, University of Göttingen, Göttingen, **1997**.
[12] SHELXL-97, Program for Crystal Structure Refinement, G. M. Sheldrick, University of Göttingen, Göttingen, **1997**.
[13] A. Boultif, D. Louër, *J. Appl. Crystallogr.* **2004**, *37*, 724–731.
[14] a) J. Rodriguez-Carvajal, FULLPROF—A Program for Rietveld Refinement and Pattern Matching Analysis, Abstract of the Satellite Meeting on Powder Diffraction of the XV Congress of the IUCR, Toulouse, **1990**, 127; b) T. Roisnel, J. Rodriguez-Carvajal, WinPLOTR [June 2005]—A Windows Tool for Powder Diffraction Pattern Analysis. Materials Science Forum, Proceedings of the Seventh

 © 2010 Wiley-VCH Verlag GmbH & Co. KGaA, Weinheim

European Powder Diffraction Conference (EPDIC 7), Ed. R. Delhez and E. J. Mittenmeijer **2000**, 118–123.

[15] J. Laugier, B. Bochu, CHECKCELL—A Software Performing Automatic Cell/Space Group Determination, Collaborative Computational Project Number 14 (CCP14), Laboratoire des Matériaux et du Génie Physique de L′Ecole Supérieure de Physique de Grenoble (INPG), France **2000**.

[16] G. Caglioti, A. Paoletti, F. P. Ricci, *Nucl. Instrum.* **1958**, *3*, 223–228.

[17] V. Macho, L. Brombacher, H. W. Spiess, *Appl. Magn. Reson.* **2001**, *20*, 405–432.

Received: February 18, 2010
Published online: June 11, 2010

 © 2010 Wiley-VCH Verlag GmbH & Co. KGaA, Weinheim